Title page

Highly sensitive and selective detection of ppb-level acetone sensor using $WO_3/Au/SnO_2$ ternary composite gas sensor

Xiaojie Zhu [a], Oluwafunmilola Ola [b], Cong Li [c], Weixiang Gao [a], Zhipeng Wang [c], Changqian Dai [a], Yingchang Jiang [c], Shibin Sun [a*], Xueting Chang [c*]

[a] *College of Logistics Engineering, Shanghai Maritime University, Shanghai 201306, China*

[b] *Faculty of Engineering, University of Nottingham, NG7 2RD, UK*

[c] *College of Ocean Science and Engineering, Shanghai Maritime University, Shanghai 201306, China*

* Corresponding author. E-mail: xtchang@shmtu.edu.cn; sunshibin@shmtu.edu.cn.

Abstract

Developing acetone sensors with high sensitivity and selectivity at ppb level is critical for medical diagnostics and environmental monitoring while facing serious challenges. In this work, we presented a ppb-level acetone sensor based on a WO_3/Au/SnO_2 ternary composite film with sandwich structure that was obtained by combined methods of radio-frequency (RF) magnetron sputtering and ion beam sputtering. The structural and compositional properties of the WO_3/Au/SnO_2 composite film were analyzed by electron microscopy and X-ray photoelectron spectroscopy. The WO_3/Au/SnO_2 composite sensor possessed high response (28.9 to 50 ppm), low optimum working temperature (200 °C), fast response/recovery time (5.5/10.5 s), ultralow detection limit (19.3 ppb), good repeatability, and ideal long-term stability. The excellent gas-sensing performance of WO_3/Au/SnO_2 composite sensor could be mainly attributed to the construction of the heterostructures between different components and the chemical sensitization effect of the noble metal Au interlayer.

Keywords: WO_3/Au/SnO_2 composite; Acetone sensor; Sputtering; Ppb-level; Heterostructures.

1. Introduction

Acetone is a colorless, toxic, flammable, and explosive volatile organic compound (VOC) that is widely used in medical, chemical, and scientific research industries [1, 2]. Prolonged exposure to acetone at concentrations above 173 ppm can cause significant damage to the central nervous system, respiratory system, and kidneys [3, 4]. Moreover, acetone can be regarded as a specific respiratory biomarker in patients with type I diabetes mellitus. Type I diabetes can be diagnosed when the exhaled acetone concentration exceeds 1.8 ppm (the concentration of acetone in the respiratory system of a healthy human is about 0.3-0.9 ppm) [5-7]. Therefore, in order to ensure human health and environmental safety, it is of great practical significance to design an acetone sensor that can realize the detection of low concentrations.

Currently, metal oxide semiconductors (MOSs) have attracted enormous interest in the field of gas sensors due to their variety, low cost, good chemical stability, and high mobility [8-10]. Among them, n-type WO_3 and SnO_2 have attracted considerable attention in view of their various preparation methods, controllable structure, and excellent stability [11, 12]. Some studies have shown that the composites of WO_3 and SnO_2 could further enhance the sensing performance of gas sensors through the synergistic interactions between them. For instance, Toan et al. presented a gas sensor based on a bilayer SnO_2-WO_3 nanofilm with a response of 7.1 towards 250 ppm ammonia at 300 °C [13]. Yin et al. reported a gas sensor based on the WO_3-SnO_2 nanosheet composites, which could realize the high sensitivity detection towards acetone at 260 °C (32.1 towards 50 ppm acetone) [14]. The above studies demonstrate that the composites based on WO_3 and SnO_2 have promising applications in the realm of gas sensors. Unfortunately, the optimal operating temperature of most MOS-based gas sensors is higher than 250 °C, which greatly limits their further applications.

Noble metal particles are regularly exploited to improve the gas-sensing performance of MOS materials due to their excellent chemical catalysis and electron sensitization [15-17]. Toan et al. prepared the SnO_2/Pt/WO_3 nanofilm sensor with different WO_3 thicknesses (50-260 nm) via sputtering technique, which could attain a response of 27.9 towards 100 ppm ammonia at 250 °C [18]. However, it exhibited a higher detection limit (~5 ppm). Tomer et al. developed the In-loaded WO_3/SnO_2 nanohybrid sensor by nanocasting method that showed a promising response/recovery rate (11/5 s)

and low operating temperature (200 °C) [19]. Notably, the detection limit of the In-WO_3/SnO_2 nanohybrid sensor was 1 ppm, which could not realize the detection of ppb-level acetone. Consequently, it is still a great challenge to simultaneously achieve high response, low detection limit, and fast response/recovery rate towards acetone at lower operating temperatures.

Herein, we reported the WO_3/Au/SnO_2 ternary composite film with sandwich structure was prepared by combined techniques of radio-frequency (RF) magnetron sputtering and ion beam sputtering. The composite film had high nanometer roughness with the loose and porous surface structure. Under the optimum operating temperature of 200 °C, the WO_3/Au/SnO_2 composite sensor demonstrated a response of 28.9 towards 50 ppm acetone, which was 6.3 times higher than that of the pure SnO_2 film sensor (4.6). Meanwhile, the response/recovery time was 5.5/10.5 s, and the detection limit was 170 ppb with ideal selectivity and good stability.

2. Experimental section

2.1 Chemicals and Materials

High-purity SnO_2 (99.99%), WO_3 (99.99%), and Au (99.999%) targets were purchased from ZhongNuo Advanced Material (Beijing) Technology Co., Ltd. Ar (99.999%) was provided by Shanghai Canghai Industrial Gas Co., Ltd. Planar electrodes were obtained from Beijing Airit Technology Co., Ltd. Isopropanol (99.7 %), ammonia (28 %), acetone (99.5 %), and formaldehyde (38 %) were obtained from Sinopharm Chemical Reagent Co., Ltd. All chemicals were used directly without further purification.

2.2 Sample preparation

The pure SnO_2 film on the planar electrode was first fabricated by an RF magnetron sputtering system (JCP350, Beijing Technol. Science Co., Ltd). The deposited parameters of the SnO_2 film were as follows: base chamber pressure: 7.8×10^{-4} Pa, Ar flow rate: 23.5 sccm, sputtering pressure: 1.7 Pa, sputtering power: 100 W, substrate rotation rate: 10 rpm, sputtering time: 30 min. The Au/SnO_2 film was then obtained by depositing Au nanoparticles on the surface of the SnO_2 film using an ion beam sputtering system (EM ACE600, Leica Co., Ltd). The sputtering parameters of the Au nanoparticles were as follows: base chamber pressure: 5×10^{-4} Pa, sputtering current: 30 mA, sputtering time: 5 min, thickness: 6 nm. The WO_3/Au/SnO_2 ternary composite film was prepared by continuing to deposit the

WO_3 film onto the Au/SnO_2 film. The deposition process of the WO_3 film was similar to that of the SnO_2 film, except the sputtering time was changed to 4 min. Finally, the as-deposited SnO_2 film, Au/SnO_2 film, and WO_3/Au/SnO_2 ternary composite film were annealed in a tube furnace for 3 h at 350 °C with a heating rate of 5 °C/min in air.

2.3 Characterization

The surface morphology and microstructure of the as-deposited film samples were observed by scanning electron microscopy (SEM, ZEISS Gemini 300, Germany) at an accelerating voltage of 20 kV. The elemental composition and distribution were investigated using an energy dispersive spectroscopy (EDS) equipped inside the SEM instrument. The chemical compositions were analyzed by X-ray photoelectron spectroscopy (XPS, ESCALAB 250 XI, ThermoFisher Scientific, USA) with Al Kα radiation source (hν = 1486.6 eV).

2.4 Gas-sensing measurements

The gas-sensing properties of the SnO_2 film, Au/SnO_2 film, and WO_3/Au/SnO_2 ternary composite film-based sensors were tested on a static testing instrument with 18 L sensing test chamber (WS-30A, Zhengzhou Winsen Electronics Technology Co., Ltd.). All gas-sensing tests were performed at room temperature (26 °C) and the relative humidity (RH) in the test chamber was maintained at 45%. The four Pt wire pins of the as-deposited planar electrodes were soldered onto the sensor bases. The operating temperature of the sensors could be adjusted by controlling the voltage of the Ru heating resistor on the backside of the planar electrode. The as-prepared gas sensors were connected to the 32-channel sensor sockets in the chamber of the WS-30A testing system. The test gases were typical VOCs, including isopropanol, ammonia, acetone, and formaldehyde. During the testing, the liquid VOCs were injected with a microsyringe onto the evaporator inside the test chamber to form vaporized gas. A hygrometer was used to monitor changes of RH inside the test chamber in real time. The response of the gas sensor was defined as $S = R_a/R_g$, where R_a and R_g were the resistances of the sensor in air and test gases, respectively. The response (T_{res}) and recovery times (T_{rec}) of the gas sensor were calculated as the time required for the test gas adsorption and desorption to achieve 90% of the resistance change, respectively.

3. Results and discussion

3.1 Characterization

Fig. 1 shows the SEM images of the prepared SnO_2 film, Au/SnO_2 film, and WO_3/Au/SnO_2 ternary composite film. As can be seen from Fig. 1a, the surface of the SnO_2 film comprised a large number of irregular particles of different sizes (several micrometers) and shapes, which had obvious pores and cracks among each other. The formation of highly porous nanostructures on the film surface could be attributed to the decrease in the mobility of adsorbed atoms during the sputtering process [20]. The high-resolution SEM image of the SnO_2 film shown in Fig. 1b further demonstrates the particle structure composed of numerous uniformly sized nanocluster aggregates. As a result, the SnO_2 film exhibited high surface nanoroughness. Figs. 1c-f shows the SEM images of the Au/SnO_2 film and WO_3/Au/SnO_2 ternary composite film. It can be observed that the surface of the Au/SnO_2 film and WO_3/Au/SnO_2 ternary composite film still showed a porous structure similar to the SnO_2 film. Notably, the nanoroughness of the surface of the WO_3/Au/SnO_2 ternary composite film further increased after deposition of Au nanoparticles and WO_3 layers. This may be due to the multilayer deposition effect of WO_3, Au, and SnO_2, which resulted in the formation of more complex and inhomogeneous nanostructures on the surface of the ternary composite film, thus increasing the surface roughness.

As shown by the cross-sectional SEM image in Fig. 1g, the pure SnO_2 film exhibited a relatively homogeneous structure with excellent film thickness consistency, and the average thickness was about 320 nm. As observed in Fig. 1h, the WO_3/Au/SnO_2 ternary composite film presented an obvious bilayer structure with an average thickness of about 400 nm. Moreover, the average thickness of the pure WO_3 film was about 73 nm (inset in Fig. 1h). It could thus be confirmed that the thickness of the Au nanoparticle layer was about 7 nm, which is approximately the same as the deposited thickness of the Au nanoparticle layer (6 nm) of the ion beam sputtering system setup. It is noteworthy that the thickness of the Au nanoparticle layer could not be directly and clearly observed by Fig. 1h, which was attributed to its exceptionally thin thickness. The EDS mapping image in Fig. 1i demonstrates the uniform distribution of W, O, Au, and Sn elements in the ternary composite film, confirming the successful preparation of the WO_3/Au/SnO_2 ternary composite film.

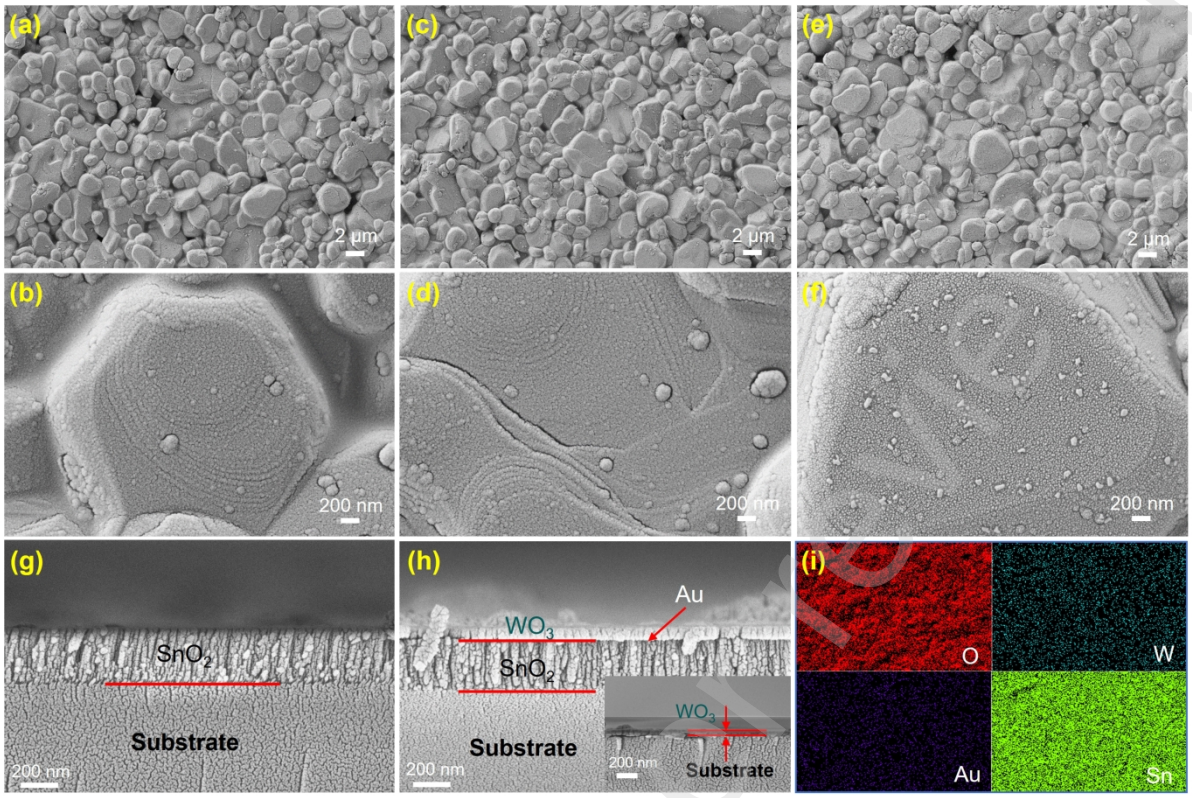

Fig. 1. SEM images of (a, b) SnO_2 film, (c, d) Au/SnO_2 film, and (e, f) WO_3/Au/SnO_2 film. Cross-sectional SEM images of (g) SnO_2 film and (h) WO_3/Au/SnO_2 film. Inset in Fig. 1h is the cross-sectional SEM image of WO_3 film. (i) EDS element mapping images of WO_3/Au/SnO_2 film.

As shown in Fig. 2a, the XPS spectral analysis of the WO_3/Au/SnO_2 ternary composite film clearly shows the characteristic peaks corresponding to Sn, Au, W, and O elements, which coincided with the EDS analysis results (Fig. 1i). Fig. 2b shows the Sn 3d spectra of the WO_3/Au/SnO_2 ternary composite film present two distinct characteristic peaks at 495.1 and 486.7 eV, corresponding to the Sn $3d_{3/2}$ and Sn $3d_{5/2}$ of the Sn^{4+} oxidation state of SnO_2, respectively [21, 22]. In Fig. 2c, the Au 4f spectra can be observed with Au $4f_{7/2}$ (84.0) and Au $4f_{5/2}$ (87.7 eV) characteristic peaks, demonstrating that the Au in the composite film exists in a metallic (Au^0) state [23, 24]. As observed in Fig. 2d, the W 4f spectra shows two distinctive peaks at 35.6 and 37.8 eV binding energies, corresponding to the W $4f_{7/2}$ and W $4f_{5/2}$, respectively, indicating that W is the oxidation state of W^{6+} [25-27]. For the O 1s spectra in Fig. 2e, the O 1s peak exhibits an asymmetry that can be decomposed into two peaks of different oxygen types. Among them, the peak with lower binding energy (530.5 eV) represents lattice oxygen (O_L), while the peak with higher binding energy (532.0 eV) represents chemisorbed oxygen (O_C) [28, 29].

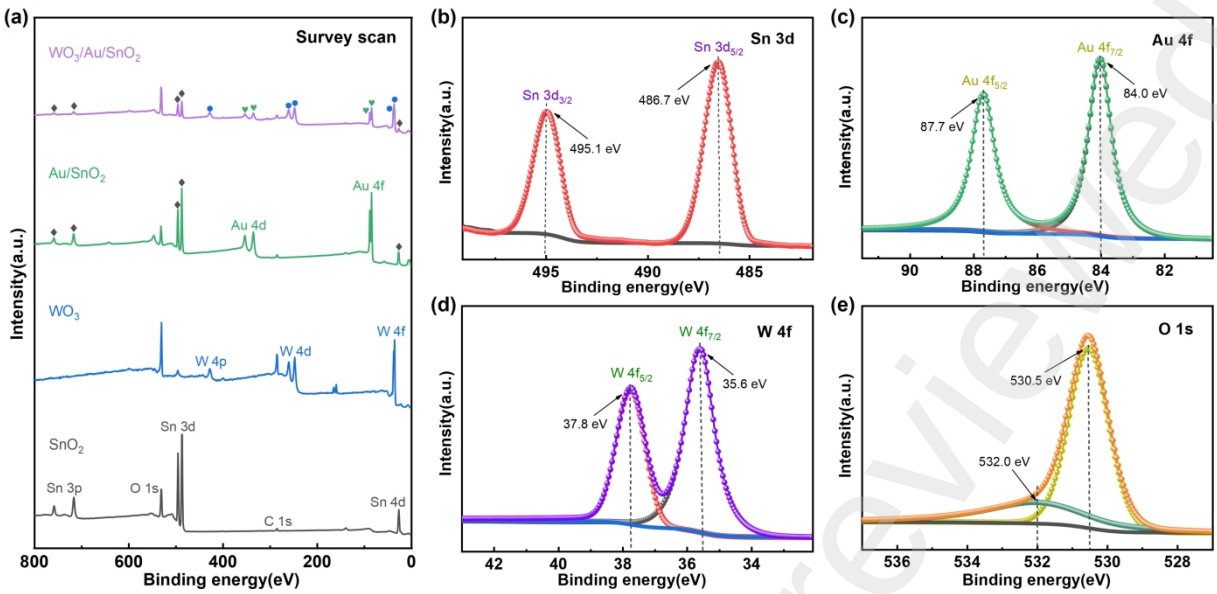

Fig. 2. (a) Survey XPS spectra of SnO_2 film, WO_3 film, Au/SnO_2 film, and WO_3/Au/SnO_2 film. Spectra of WO_3/Au/SnO_2 film: (b) Sn 3d, (c) Au 4f, (d) W 4f, and (e) O 1s.

3.2 Gas-sensing performance

Figs. 3a-f shows the dynamic response-recovery curves of the SnO_2, Au/SnO_2, and WO_3/Au/SnO_2 sensors towards 50 ppm acetone at different operating temperatures (160-260 °C). It can be observed that the resistance of all the sensors decreased rapidly when exposed to acetone, and the resistance quickly recovered to the initial value after re-exposure to air. This response phenomenon indicates that all three sensors exhibited n-type semiconductor behaviors. Fig. 3g displays the original resistance of different sensors in air in the range of 160-260 °C. It is clear that the resistance of all sensors tended to decrease as the operating temperature increased, which can be attributed to the increase of the carrier density at high temperatures [30, 31]. Remarkably, the increasing order of the resistance for the sensors in air at the same operating temperature was SnO_2<Au/SnO_2<WO_3/Au/SnO_2 sensors. This behavior is due to the differences in the components of the gas-sensing materials affecting their internal electron mobility and conductivity.

The variation curves of the response for each sensor to 50 ppm acetone at different operating temperatures are shown in Fig. 3h. The response of all sensors displayed a volcano-like pattern of "increase-maximum-decrease" as the operating temperature increased. This may be attributed to the impact of operating temperature on the adsorption and desorption processes of acetone on the surface of the gas-sensing materials. Obviously, the response of the WO_3/Au/SnO_2 sensor was higher than that

of the other two sensors over the entire temperature interval. The response of the WO_3/Au/SnO_2 sensor to 50 ppm acetone reached a maximum of 28.9 at 200 °C, indicating that its optimal working temperature was 200 °C. Meanwhile, the responses of the SnO_2 and Au/SnO_2 sensors were 4.6 and 9.3, respectively. Importantly, the WO_3/Au/SnO_2 sensor not only exhibited a lower optimal operating temperature but also a higher response, which was attributed to the construction of inter-component heterojunctions and the chemosensitizing effect of Au nanoparticle loading.

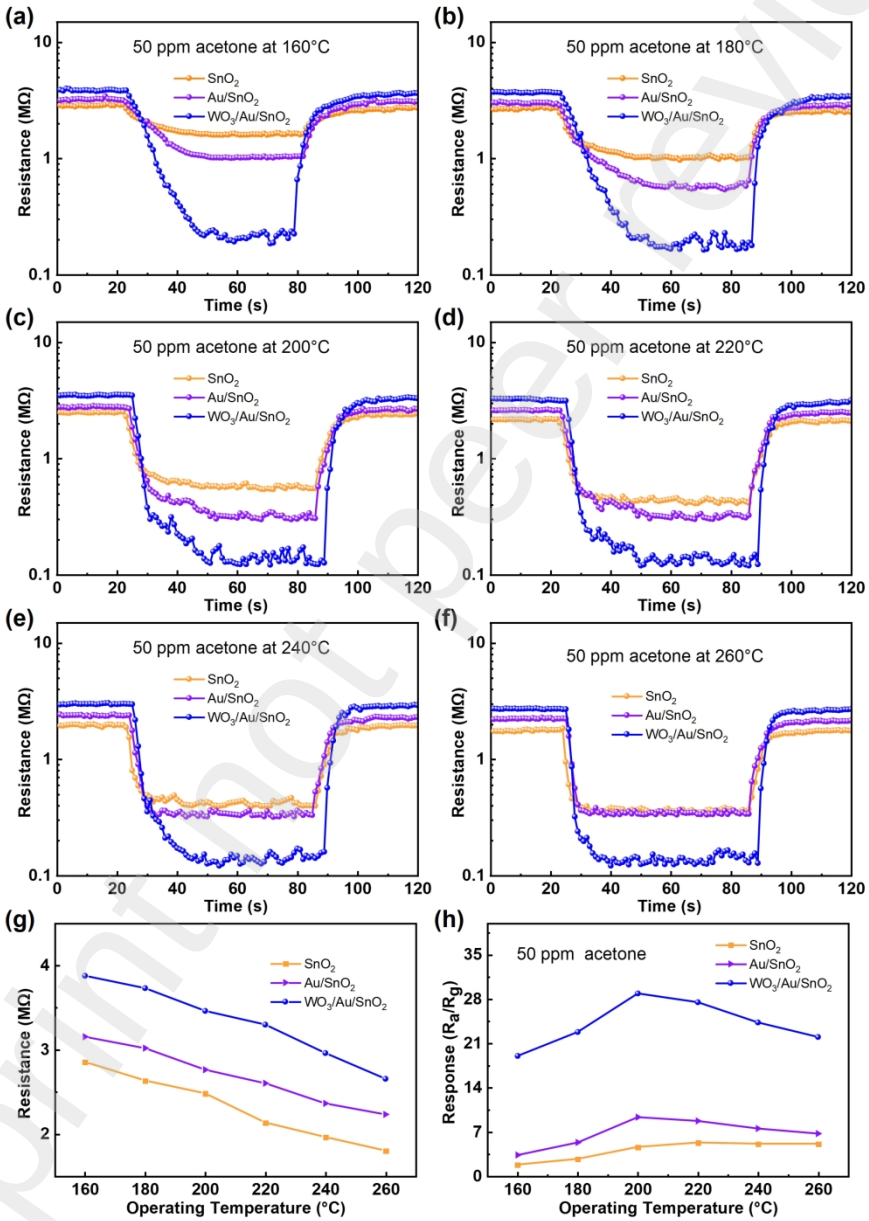

Fig. 3. Response-recovery curves of different sensors to 50 ppm acetone at (a) 160 °C, (b) 180 °C, (c) 200 °C, (d) 220 °C, (e) 240 °C, and (f) 260 °C. (g) Plots of resistances of different sensors in air at different operating temperatures. (h) Plots of responses of different sensors to 50 ppm acetone at different operating temperatures.

As shown in Fig. 4a, all sensors exhibited good response/recovery characteristics, and the responses of the sensors all increased with increasing of the acetone concentration. Among them, the response of the WO_3/Au/SnO_2 sensor was the highest at all concentrations. The inset in Fig. 4a shows the response-recovery curves of each sensor to low concentrations (0.17-5 ppm) of acetone. In particular, the response of the WO_3/Au/SnO_2 sensor to 0.17 ppm (170 ppb) acetone was 2.2, which was 1.8 and 1.6 times higher than that of the SnO_2 (1.2) and Au/SnO_2 (1.4) sensors, respectively. This means that the WO_3/Au/SnO_2 sensor could be used to diagnose patients with type I diabetes [5, 32, 33]. Based on the signal-to-noise ratio of 3σ/s, the theoretical detection limit of the WO_3/Au/SnO_2 sensor was obtained to be 19.3 ppb [34, 35].

In addition, in the low concentration range (0.17-5 ppm), the responses of all the sensors to acetone showed the good linear relationship with the concentrations, as shown in Fig. 4b. The linear fitting parameters of the SnO_2, Au/SnO_2, and WO_3/Au/SnO_2 sensors were 0.968, 0.983 and 0.991, respectively. As displayed in Fig. 4c, compared to the SnO_2 and Au/SnO_2 sensors, the response of the WO_3/Au/SnO_2 sensor increased significantly with increasing of the acetone concentration and had the higher response values. For example, the responses of the WO_3/Au/SnO_2 sensor to high concentrations (300 ppm, 400 ppm, and 500 ppm) of acetone were 53.8, 61.5, and 64.3, respectively, which were much higher than that of the Au/SnO_2 (17.7, 19.3, and 24.1) and SnO_2 sensors (8.8, 9.8, and 10.1). This amply demonstrated that the WO_3/Au/SnO_2 sensor not only had the high response towards acetone but also had the desirable low detection limit and a wide concentration detection range. The acetone-sensing performance of the WO_3/Au/SnO_2 sensor was compared in detail with other reported gas sensors, as shown in Table 1 [7, 30, 36-40]. Evidently, the WO_3/Au/SnO_2 sensor showed greater competitiveness in terms of optimal operating temperature, detection limit, and response value compared to other sensors.

Figs. 4d and e shows the response/recovery times of the SnO_2 and WO_3/Au/SnO_2 sensors to 50 ppm acetone at 200 °C, respectively. As can be seen from Fig. 4d, the recovery/response time of the SnO_2 sensor to 50 ppm acetone was 10.2/17.1 s. In contrast, the response/recovery rate of the WO_3/Au/SnO_2 sensor was considerably faster than the SnO_2 sensor, and its recovery/response time was reduced to 5.5/10.5 s, respectively, as shown in Fig. 4e. The ideal response/recovery rate of the WO_3/Au/SnO_2

sensor to acetone indicates that it can fully realize the requirements of practical applications.

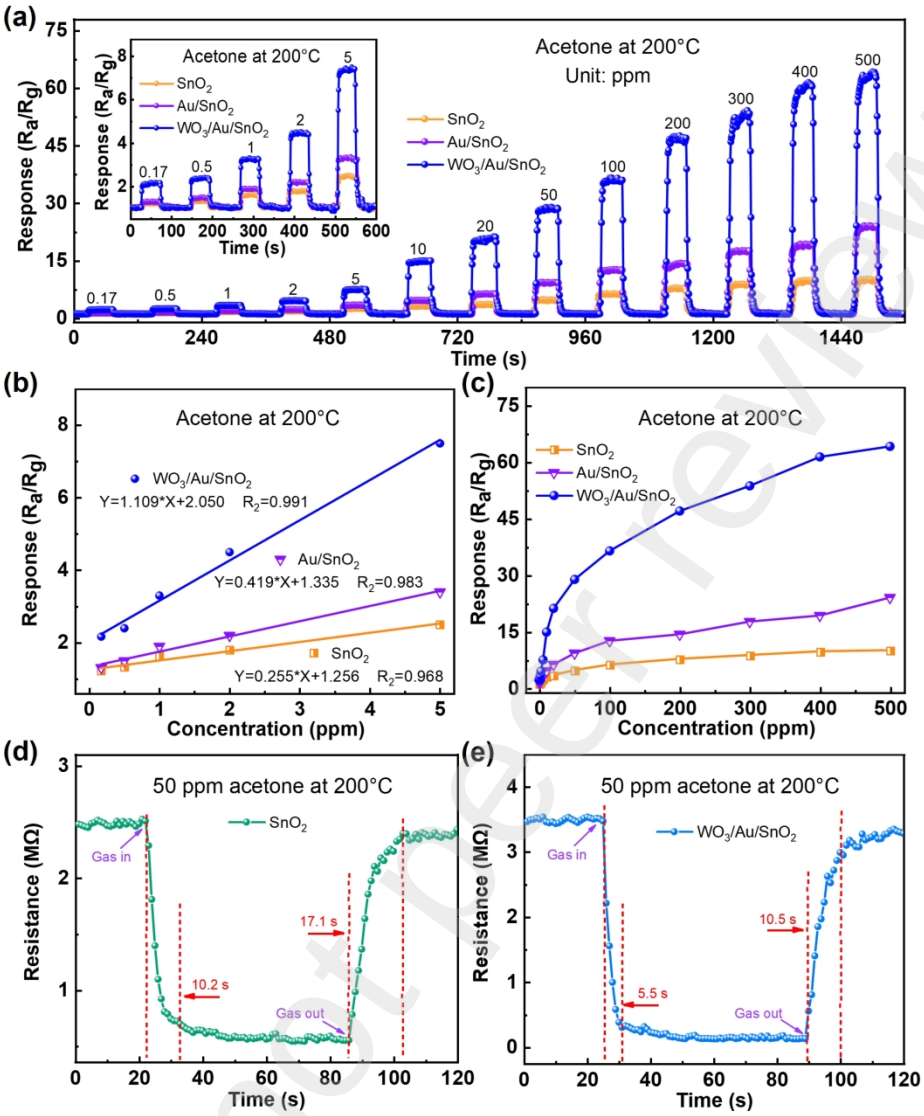

Fig. 4. (a) Response-recovery curves of different sensors to 0.17-500 ppm acetone at 200 °C. Inset in Fig. 4a is the enlarged response-recovery curves to 0.17-5 ppm acetone. (b) Response-concentration relationships of different sensors. (c) Plots of responses for different sensors as a function of acetone concentration (0.17-500 ppm). (d, e) Response and recovery times of the SnO_2 and $WO_3/Au/SnO_2$ sensors to 50 ppm acetone at 200 °C.

Table 1. Comparison of acetone-sensing performance of WO_3/Au/SnO_2 sensor with other reported gas sensors.

Materials	T (°C)	Con. (ppm)	Res. (R_a/R_g)	T_{res}/T_{rec}	Det. Lim. (ppm)	Ref.
Au/SnO_2 nanosheets	240	100	18.2	5/66	1	[7]
TiO_2/g-C_3N_4/POM nanofibers	330	100	10.5	1/16	-	[30]
Co_3O_4 nanowire arrays	200	100	16.7	4/39	1	[36]
WO_3 powder	200	100	28.7	3/113	2	[37]
Hierarchy porous TiO_2 nanosheets	400	200	21.6	0.75/0.5	0.5	[38]
ZnO/Co_3O_4 hollow polyhedron	300	100	30	8/2	1	[39]
Co_3O_4 nanoparticles	200	50	7.35	43/92	0.1	[40]
WO_3/Au/SnO_2 ternary composite film	200	50	28.9	5.5/10.5	0.17	This work

Figs. 5a-c shows the response-recovery curves of the SnO_2, Au/SnO_2, and WO_3/Au/SnO_2 sensors to 50 ppm formaldehyde, isopropanol, and ammonia at 200 °C, respectively. It can be clearly seen that all the sensors exhibited significant responses to the above three VOCs with fast response/recovery rates. As displayed in Fig. 5d, the response of the WO_3/Au/SnO_2 sensor to acetone was significantly higher than the other three VOCs. The response of the WO_3/Au/SnO_2 sensor to 50 ppm acetone at 200 °C was 28.9, which was 2.2, 1.6, and 2.7 times higher than that to formaldehyde (13.1), ammonia (18), and isopropanol (10.8), respectively. Moreover, the WO_3/Au/SnO_2 sensor also had superior response performance compared with the SnO_2 and Au/SnO_2 sensors. The results showed that the WO_3/Au/SnO_2 sensor had the best selectivity to acetone, as well as a desirable anti-interference ability for other gases.

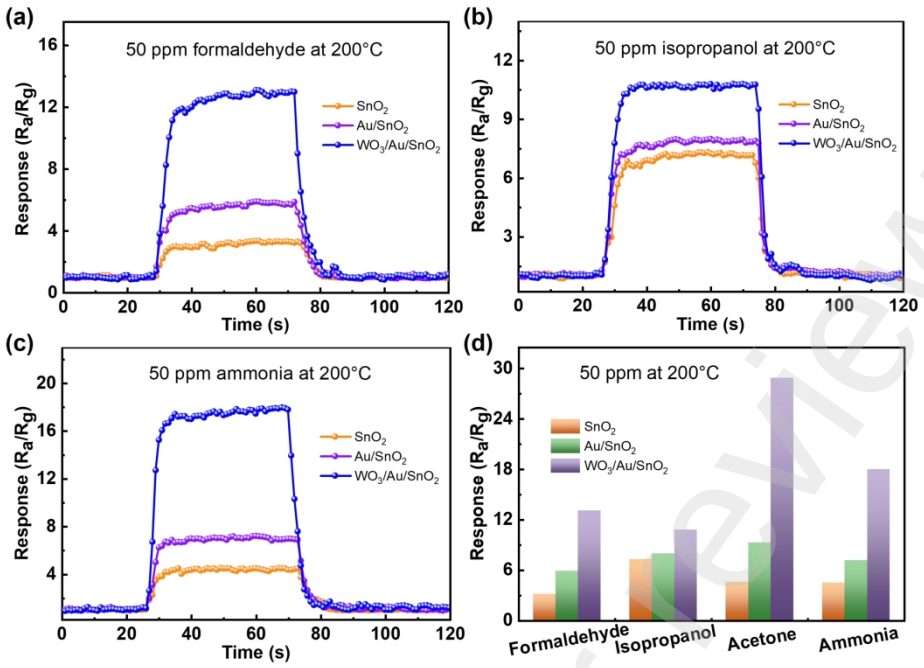

Fig. 5. Response-recovery curves of different sensors to 50 ppm (a) formaldehyde, (b) isopropanol, and (c) ammonia at 200 °C. (d) Selectivity of different sensors to different VOCs (50 ppm) at 200 °C.

Fig. 6a displays the repeatability of the WO_3/Au/SnO_2 sensor to 50 ppm acetone for 100 consecutive tests at 200 °C. Apparently, the response-recovery curves fluctuated less and the response values decayed very slightly, which proved that the WO_3/Au/SnO_2 sensor had excellent reproducibility. Fig. 6b records the response-recovery curves of the WO_3/Au/SnO_2 sensor for a long-term follow-up test to 50 ppm acetone over 30 days. It can be observed that the WO_3/Au/SnO_2 sensor still retained the high response to acetone after up to 30 days of testing. The above results confirmed that the WO_3/Au/SnO_2 sensor had good repeatability, ideal long-term stability, and durability, which also ensured its reliability in practical application environments.

Fig. 6c presents the response-recovery curves of the WO_3/Au/SnO_2 sensor to 50 ppm acetone at 200 °C in the range of 10-96% RH. The responses of the WO_3/Au/SnO_2 sensor showed a tendency to decrease with increasing RH, but the response/recovery rates did not change significantly. The response of the WO_3/Au/SnO_2 sensor with varying RH could be roughly categorized into three phases. Within 10-30 % RH, the response of the WO_3/Au/SnO_2 sensor decreased from 36.1 to 34, indicating that lower RH had insignificant effect on the performance of the sensor. When the RH increased from 40 to 70%, the response of the WO_3/Au/SnO_2 sensor decreased sharply from 29.6 to 16.2. This can be

attributed to the water molecules occupying the active sites on the surface of the WO_3/Au/SnO_2 ternary composite film, hindering the reaction between oxygen ions and acetone molecules [41]. Moreover, the water molecules can also react with chemisorbed oxygen ions on the surface of the film to form terminal hydroxyl groups, reducing the resistance of the sensor, which ultimately significantly reduces the response of the sensor [42]. In the range of 80-96% RH, the response of the sensor slowly decayed from 14.5 to 13.2. This phenomenon may be attributed to the saturation of water molecules adsorbed on the surface of the film in high RH environments, which has insignificant effect on the response of the sensor.

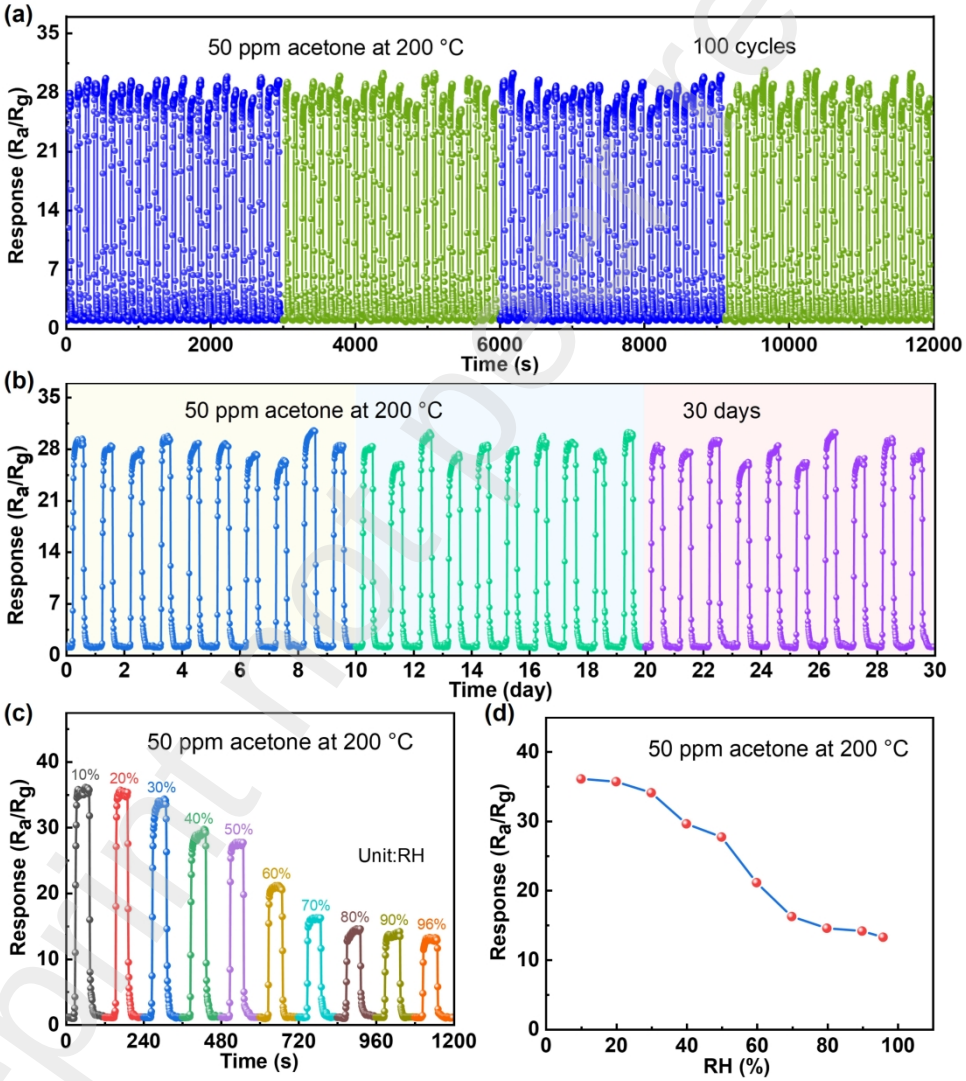

Fig. 6. (a) Cyclic response-recovery curves of WO_3/Au/SnO_2 sensor to 50 ppm acetone at 200 °C. (b) Long-term stability of WO_3/Au/SnO_2 sensor. (c) Response-recovery curves of WO_3/Au/SnO_2 sensor under different RH and the RH setting temperature of 26 °C. (d) Plot of WO_3/Au/SnO_2 sensor responses as a function of RH.

3.3 Gas-sensing mechanism

As widely recognized, the gas-sensing mechanism of the MOS-based sensors is the redox reaction between target gas and chemically adsorbed oxygen (O_2^-, O^- and O^{2-}) on the surface of the gas-sensing material, leading to the change of the sensor resistance [43, 44]. Fig. 7a shows the schematic of the acetone-sensing mechanism of the WO_3/Au/SnO_2 sensor. When the WO_3/Au/SnO_2 sensor exposed in air, the oxygen molecules on the surface of the film could capture electrons from the conduction band of the oxide semiconductors to form chemisorbed oxygen ions (O^-) (100-300 °C) [45], as expressed by Eqs. (1)-(3):

$$O_2\,(gas) \rightarrow O_2\,(ads) \quad (1)$$

$$O_2\,(ads) + e^- \rightarrow O_2^-\,(ads) \quad (2)$$

$$O_2^-\,(ads) + e^- \rightarrow 2O^-\,(ads) \quad (3)$$

The migration of electrons occurs causing an electron depletion layer on the surface of the film, which caused the WO_3/Au/SnO_2 sensor in a high-resistance state. When the WO_3/Au/SnO_2 sensor was exposed to acetone, the acetone molecules would undergo a redox reaction with the O^- on the surface of the film, releasing electrons back into the conduction band of the oxide semiconductors. This resulted in a narrowing of the electron depletion layer on the surface of the film, which led to the lower resistance of the WO_3/Au/SnO_2 sensor. The reaction process could be expressed by Eq. (4):

$$CH_3COCH_3\ (gas) + 8O^-\ (ads) \rightarrow 3CO_2 + 3H_2O + 8e^- \quad (4)$$

Compared to the SnO_2 and Au/SnO_2 sensors, the acetone-sensing performance of the WO_3/Au/SnO_2 sensor improved significantly, which could be mainly attributed to the following reasons:

First, the compositing of WO_3, Au, and SnO_2 formed heterojunctions at the contact interface with each other, which significantly improved the acetone-sensing performance of the WO_3/Au/SnO_2 sensor. As shown in Fig. 7b, the work functions of WO_3, Au, and SnO_2 are 5.25, 5.1, and 4.9, respectively [27, 46, 47]. When the WO_3/Au/SnO_2 sensor was in air, the electrons migrated from SnO_2 to Au, while the electrons in Au migrated to WO_3, until the Fermi-level reached equilibrium. At this time, the electron depletion layers were created at the interface of the three materials, resulting in an increase in the resistance of the WO_3/Au/SnO_2 sensor (Fig. 7c). When the WO_3/Au/SnO_2 sensor was contacted with acetone, the acetone molecules reacted with O^-, releasing electrons back into the

conduction band of the film, leading to the narrowing of the electron depletion layers at the interfaces, and ultimately resulting in the decrease of the resistance of the WO_3/Au/SnO_2 sensor, as depicted in Fig. 7d. For the above reason, the WO_3/Au/SnO_2 sensor could cause more remarkable resistance changes than the SnO_2 and Au/SnO_2 sensors, demonstrating superior gas-sensing performance for acetone.

Then, the Au nanoparticles loaded in the WO_3/Au/SnO_2 ternary composite film played an important role to enhance the acetone-sensing performance of the sensor through the mechanism of chemical sensitization. Au nanoparticles have excellent catalytic activity, which can promote the decomposition of acetone molecules into more active radical groups, reduce the activation energy of the reaction, and generate more reactive chemisorbed oxygen ions [48, 49]. These additional adsorbed oxygen ions (O^-) on the surface of the film could react with more acetone molecules, thus effectively improving the gas-sensing performance of the WO_3/Au/SnO_2 sensor.

Finally, the SEM analysis results (Figs. 1e, f) showed that the porous structure and high nanoroughness surface of the WO_3/Au/SnO_2 ternary composite film provided more adsorption and reactive sites to acetone molecules in certain degree, which served to enhance the gas-sensing performance of the WO_3/Au/SnO_2 sensor.

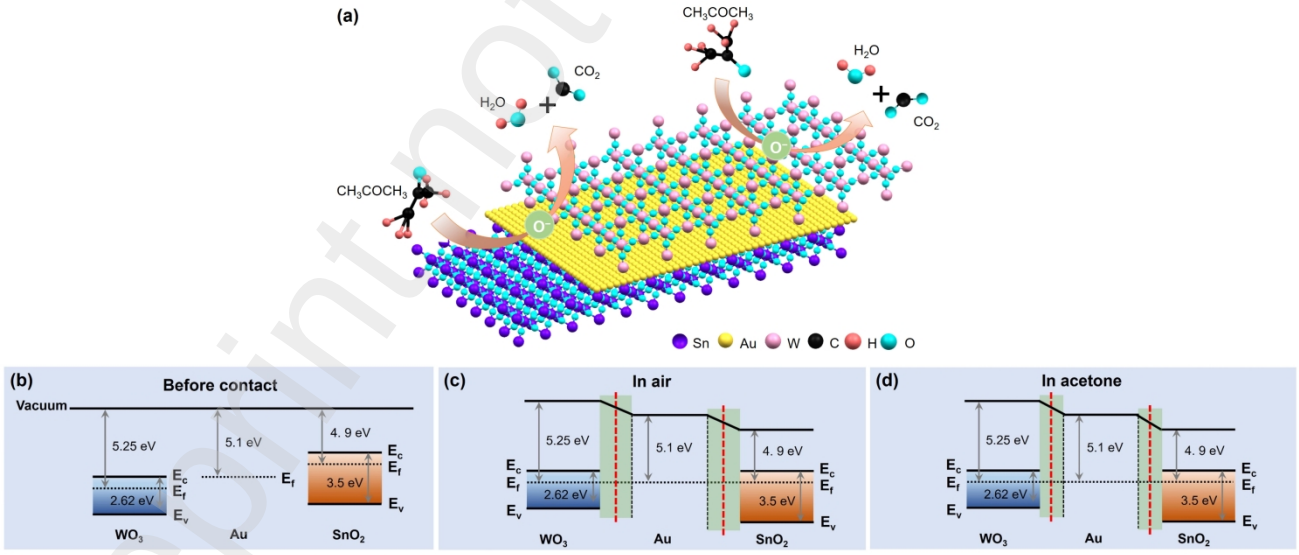

Fig. 7. Schematic diagram of acetone-sensing mechanism of WO_3/Au/SnO_2 sensor.

4. Conclusions

In summary, the WO_3/Au/SnO_2 ternary composite film with sandwich structure was alternately

deposited by RF magnetron sputtering and ion beam sputtering. The surface of the as-deposited ternary composite film had high nanoroughness with a large number of porous structure favorable for the adsorption and diffusion of acetone molecules. The WO_3/Au/SnO_2 ternary composite film exhibited high response (28.9 to 50 ppm acetone), fast response/recovery rates (5.5/10.5 s), very low experimental and theoretical detection limits (170/19.3 ppb), good repeatability and reliable long-term stability. This work provides new ideas for the development of ppb-level acetone sensors based on the noble metal and MOS composites.

Acknowledgements

This work is financially supported by the National Natural Science Foundation of China (52172094), the Royal Society International Exchanges Cost Share (NSFC) IEC\NSFC\223453, the Shanghai Municipal Natural Science Foundation (21ZR1426700), the International Science and Technology Cooperation Program (CU03-29), the "Shuguang" Program of Shanghai Education Commission (19SG46), and the Shanghai Engineering Technology Research Center Program (19DZ2253100).

Reference

[1] C.Y. Li, K. Kim, T. Fuchigami, T. Asaka, K. Kakimoto, Y. Masuda, Acetone gas sensor based on Nb_2O_5@SnO_2 hybrid structure with high selectivity and ppt-level sensitivity, Sens. Actuators B Chem. 393 (2023) 134144.

[2] L.B. Cai, X.Q. Dong, G.G. Wu, J.P. Sun, N. Chen, H.Z. Wei, S. Zhu, Q.Y. Tian, X.Y. Wang, Q. Jing, P. Li, B. Liu, Ultrasensitive acetone gas sensor can distinguish the diabetic state of people and its high performance analysis by first-principles calculation, Sens. Actuators B Chem. 351 (2022) 130863.

[3] M. Liu, J. Ji, P. Song, M. Liu, Q. Wang, α-Fe_2O_3 nanocubes/$Ti_3C_2T_x$ MXene composites for improvement of acetone sensing performance at room temperature, Sens. Actuators B Chem. 349 (2021) 130782.

[4] L. Lv, P.F. Cheng, Y. Zhang, Y.Q. Zhang, Z.H. Lei, Y.L. Wang, L.P. Xu, Z. Weng, C. Li, Ultra-high response acetone gas sensor based on $ZnFe_2O_4$ pleated hollow microspheres prepared by green NaCl template, Sens. Actuators B Chem. 358 (2022) 131490.

[5] H.Y. Lee, J.H. Bang, S.M. Majhi, A. Mirzaei, K.Y. Shin, D.J. Yu, W. Oum, S. Kang, M.L. Lee, S.S. Kim, H.W. Kim, Conductometric ppb-level acetone gas sensor based on one-pot synthesized Au@Co_3O_4 core-shell nanoparticles, Sens. Actuators B Chem. 359 (2022) 131550.

[6] S. Joshi, S. Tonde, U. Wakhure, D. Bornare, A. Chatterjee, K. Syed, M.V. Sunkara, Hierarchical

$CaTiO_3$ microspheres for acetone sensing, Sens. Actuators B Chem. 359 (2022) 131621.
[7] L.L. Guo, Z. Shen, C.H. Ma, C.Q. Ma, J.Q. Wang, T.X. Yuan, Gas sensor based on MOFs-derived Au-loaded SnO_2 nanosheets for enhanced acetone detection, J. Alloy. Compd. 906 (2022) 164375.
[8] R.L. Ma, W.C. Gan, Y.H. Zeng, S.L. Feng, S.K. Duan, P. Feng, X.Y. Peng, High-performance gas sensor utilizing g-C_3N_4/In_2O_3 composite for low concentration prediction to NO_2, Sens. Actuators B Chem. 414 (2024) 135879.
[9] D. Wang, C.S. Han, C.X. Zheng, H.R. Fang, D.F. Xu, H.B. Zhao, Fabrication of a ppb-level NO_2 gas sensor by sensitizing nanobundles assembled by In_2O_3 nanotubes with TiO_2 quantum dots, Sens. Actuators B Chem. 387 (2023) 133833.
[10] H.W. Long, Y.Q. Li, K. Chai, W. Zeng, Metal oxide semiconductor-based core-shell nanostructures for chemiresistive gas sensing: A review, Sens. Actuators B Chem. 417 (2024) 136183.
[11] L. Piliai, T.N. Dinhová, M. Janata, D. Balakin, S. Vallejos, J. Otta, J. Štefková, L. Fišer, P. Fitl, M. Novotný, J. Hubálek, M. Vorochta, I. Matolinová, M. Vrňata, NAP-XPS study of surface chemistry of CO and ethanol sensing with WO_3 nanowires-based gas sensor, Sens. Actuators B Chem. 397 (2023) 134682.
[12] L.W. Zhang, J.M. Tian, Y.T. Wang, T.Q. Wang, M.J. Wei, F. Li, D. Li, Y. Yang, H. Yu, X.T. Dong, Polyoxometalates electron acceptor-intercalated In_2O_3@SnO_2 nanofibers for chemiresistive ethanol gas sensors, Sens. Actuators B Chem. 410 (2024) 135728.
[13] N.V. Toan, C.M. Hung, N.V. Duy, N.D. Hoa, D.T.T. Le, N.V. Hieu, Bilayer SnO_2-WO_3 nanofilms for enhanced NH_3 gas sensing performance, Mater. Sci. Eng. B. 224 (2017) 163-170.
[14] M.L. Yin, Y. Yao, H.B. Fan, S.Z. Liu, WO_3-SnO_2 nanosheet composites: Hydrothermal synthesis and gas sensing mechanism, J. Alloy. Compd. 736 (2018) 322-331.
[15] L. Chen, J. Xie, Z.Y. Wang, Y.N. Zhao, J.M. Gou, J.T. Wu, Amorphous Pt-decorated α-Fe_2O_3 sensor with superior triethylamine sensing performance prepared by a one-step impregnation method, J. Alloy. Compd. 976 (2024) 173330.
[16] M.S. Nam, J.Y. Kim, A. Mirzaei, M.H. Lee, H.W. Kim, S.S. Kim, Au- and Pt-decorated $Ti_3C_2T_x$ MXenes for preparing self-heated and flexible NH_3 gas sensors, Sens. Actuators B Chem. 403 (2024) 135112.
[17] C.X. Sun, J.K. Shao, G.F. Pan, X.L. Yang, Triethylamine gas sensor based on Zn_2SnO_4 polyhedron decorated with Au nanoparticles and density functional theory investigation, Sens. Actuators B Chem. 408 (2024) 135510.
[18] N.V. Toan, C.M. Hung, N.D. Hoa, N.V. Duy, D.T.T. Le, N.T.T. Hoa, N.N. Viet, P.H. Phuoc, N.V. Hieu, Enhanced NH_3 and H_2 gas sensing with H_2S gas interference using multilayer SnO_2/Pt/WO_3 nanofilms, J. Hazard. Mater. 412 (2021) 125181.
[19] V.K. Tomer, K. Singh, H. Kaur, M. Shorie, P. Sabherwal, Rapid acetone detection using indium loaded WO_3/SnO_2 nanohybrid sensor, Sens. Actuators B Chem. 253 (2017) 703-713.
[20] H.S. Al-Salman, M.J. Abdullah, Hydrogen gas sensing based on ZnO nanostructure prepared by

RF-sputtering on quartz and PET substrates, Sens. Actuators B Chem. 181 (2013) 259-266.
[21] X.Y. Miao, L.Y. Zhu, X.Y. Wu, L.W. Mao, X.H. Jin, H.L. Lu, Precise preparation of α-Fe_2O_3/SnO_2 core-shell nanowires via atomic layer deposition for selective MEMS-based H_2S gas sensor, Sens. Actuators B Chem. 378 (2023) 133111.
[22] P. Wu, Y. Li, S. Xiao, D.C. Chen, J.Y. Chen, J. Tang, X.X. Zhang, Room-temperature detection of perfluoroisobutyronitrile with SnO_2/$Ti_3C_2T_x$ gas sensors, ACS Appl. Mater. Interfaces. 14 (2022) 48200-48211.
[23] M. Punginsang, D. Zappa, E. Comini, A. Wisitsoraat, G. Sberveglieri, A. Ponzoni, C. Liewhiran, Selective H_2S gas sensors based on ohmic hetero-interface of Au-functionalized WO_3 nanowires, Appl. Surf. Sci. 571 (2022) 151262.
[24] P.J. Guo, F.X. Yin, Z.Y. Ni, G.R. Li, B.H. Chen, MIL-101(Fe) supported Au-Cu nanoalloy for enhanced electrochemical nitrogen fixation in gas-liquid-solid three-phase reactor, Chem. Eng. J. 494 (2024) 153134.
[25] T. Wang, L.C. Huang, H.L. Wu, W.J. Li, Q. Lu, R. Han, X.S. Liang, F.M. Liu, F.M. Liu, B. Wu, G.Y. Lu, $Ce_{0.8}Gd_{0.2}O_{1.95}$ based mixed potential gas sensor: AgRu bimetallic co-regulated WO_3 for H_2 sensing under high temperature, Sens. Actuators B Chem. 402 (2024) 135105.
[26] Y. Wang, S.Y. Zhang, D.K. Xiao, S.J. Wang, T. Zhang, X. Yang, S.Q. Heng, M.J. Sun, CuO/WO_3 hollow microsphere P-N heterojunction sensor for continuous cycle detection of H_2S gas, Sens. Actuators B Chem. 374 (2023) 132823.
[27] Z. Li, D.Z. Zhang, X.W. Wang, X.C. Liu, Y. Yang, C. Du, J.Y. Guo, Y.T. Zhang, Passive and wireless NFC tag-type trimethylamine gas detection based on WO_3/MXene composite sensors, J. Alloy. Compd. 939 (2023) 168730.
[28] G.D. Wang, T.Y. Chen, L.L. Guo, H.H. Wang, X.D. Wang, H. Zeng, Y.J. Feng, W. Zhao, Y.C. Wang, X.L. Liu, J.J. Wang, Y.L. Yang, Chemiresistive n-butanol gas sensors based on Co_3O_4@ZnO hollow-sphere-array thin films prepared by template-assisted magnetron sputtering, Sens. Actuators B Chem. 413 (2024) 135862.
[29] M. Zhang, X.T. Lv, T.Q. Wang, W.Y. Pei, Y. Yang, F. Li, D.D. Yin, H. Yu, X.T. Dong, CuO-based gas sensor decorated by polyoxometalates electron acceptors: From constructing heterostructure to improved sensitivity and fast response for ethanol detection, Sens. Actuators B Chem. 415 (2024) 136016.
[30] J.Y. Gao, Y. Yang, F. Li, D. Li, H. Yu, X.T. Dong, T.Q. Wang, Polyoxometalate electron acceptor heterogenous dopant into TiO_2/g-C_3N_4 nanofibers for promoted acetone gas detectability, Sens. Actuators B Chem. 417 (2024) 136072.
[31] Z.Y. Yuan, N.H. Chu, F.L. Meng, Improvement in the performance of In_2O_3 ethanol sensor by perovskite-type $LaFeO_3$ modification and sensitivity mechanism analysis, Sens. Actuators B Chem. 406 (2024) 135415.
[32] J.H. Kim, A. Mirzaei, I. Sakaguchi, S. Hishita, T. Ohsawa, T.T. Suzuki, S.S. Kim, N. Saito,

Decoration of Pt/Pd bimetallic nanoparticles on Ru-implanted WS_2 nanosheets for acetone sensing studies, Appl. Surf. Sci. 641 (2023) 158478.
[33] W.J. Wang, J.B. Xian, J. Li, M.F. Yu, Q.T. Duan, C.M. Leung, M. Zeng, X.S. Gao, Construction of Co_3O_4/SnO_2 yolk-shell nanofibers for acetone gas detection, Sens. Actuators B Chem. 398 (2024) 134724.
[34] T.Z. Wang, J.K. Chen, J.X. Chen, X. Yao, G. Chen, Z. Jiao, J.T. Zhao, S. Cheng. X.C. Yang, Q.L. Li, UV-light enhanced gas sensor based on Ga doped ZnO for ultra-high sensitive and selective n-butanol detection, Appl. Surf. Sci. 641 (2023) 158551.
[35] G. Gorthala, R. Ghosh, Impact of gas flowrate on performance of chemiresistive NO_2 sensors, Appl. Surf. Sci. 670 (2024) 160597.
[36] K. Xu, C. Lai, Y.X. Yang, H. Zhou, C.W. Zhou, Y. Yang, T. Yu, C.L. Yuan, Pore engineering of Co_3O_4 nanowire arrays by MOF-assisted construction for enhanced acetone sensing performances, Sens. Actuators B Chem. 329 (2021) 129095.
[37] Q. Wang, X. Cheng, Y.R. Wang, Y.F. Yang, Q. Su, J.P. Li, B.X. An, Y.B. Luo, Z.K. Wu, E.Q. Xie, Sea urchins-like WO_3 as a material for resistive acetone gas sensors, Sens. Actuators B Chem. 355 (2022) 131262.
[38] W.Y. Ge, S.Y. Jiao, Z. Chang, X.M. He, Y.X. Li, Ultrafast response and high selectivity toward acetone vapor using hierarchical structured TiO_2 nanosheets, ACS Appl. Mater. Interfaces. 12 (2020) 13200-13207.
[39] D.Z. Zhang, Z.M. Yang, Z.L. Wu, G.K. Dong, Metal-organic frameworks-derived hollow zinc oxide/cobalt oxide nanoheterostructure for highly sensitive acetone sensing, Sens. Actuators B Chem. 283 (2019) 42-51.
[40] X.X. Fan, Y.J. Xu, C.Y. Ma, W.M. He, In-situ growth of Co_3O_4 nanoparticles based on electrospray for an acetone gas sensor, J. Alloy. Compd. 854 (2021) 157234.
[41] X.P. Song, L. Li, X. Chen, Q. Xu, B. Song, Z.Y. Pan, Y.N. Liu, F.Y. Juan, F. Xu, B.Q. Cao, Enhanced triethylamine sensing performance of α-Fe_2O_3 nanoparticle/ZnO nanorod heterostructures, Sens. Actuators B Chem. 298 (2019) 126917.
[42] H.N. Bai, H. Guo, J. Wang, Y. Dong, B. Liu, F.Q. Guo, D.J. Chen, R. Zhang, Y.D. Zheng, Hydrogen gas sensor based on SnO_2 nanospheres modified with Sb_2O_3 prepared by one-step solvothermal route, Sens. Actuators B Chem. 331 (2021) 129441.
[43] S.X. Fan, W. Tang, Synthesis, characterization and mechanism of electrospun carbon nanofibers decorated with ZnO nanoparticles for flexible ammonia gas sensors at room temperature, Sens. Actuators B Chem. 362 (2022) 131789.
[44] Y.Q. Chen, Y.X. Li, B.X. Feng, Y. Wu, Y.H. Zhu, J. Wei, Self-templated synthesis of mesoporous Au-ZnO nanospheres for seafood freshness detection, Sens. Actuators B Chem. 360 (2022) 131662.
[45] S.M. Li, W.L. Zhang, C.W. Wang, G. Li, Au nanoparticles decorated $ZnIn_2S_4/WO_3$ core-shell heterostructures as highly sensitive and selective ethylene glycol gas sensors, J. Alloy. Compd. 998

(2024) 175027.
[46] J.F. Tang, C.C. Fang, C.L. Hsu, Enhanced organic gas sensor based on Cerium- and Au-doped ZnO nanowires via low temperature one-pot synthesis, Appl. Surf. Sci. 613 (2023) 156094.
[47] S. Gasso, M.K. Sohal, A. Mahajan, MXene modulated SnO_2 gas sensor for ultra-responsive room-temperature detection of NO_2, Sens. Actuators B Chem. 357 (2022) 131427.
[48] S. Yang, J. Sun, L. Xu, Q.Q. Zhou, X.F. Chen, S.D. Zhu, B. Dong, G.Y. Lu, H.W. Song, Au@ZnO functionalized three-dimensional macroporous WO_3: A application of selective H_2S gas sensor for exhaled breath biomarker detection, Sens. Actuators B Chem. 324 (2020) 128725.
[49] Y.M. Liu, X. Li, Y.L. Wang, X.W. Li, P.F. Cheng, Y. Zhao, F. Dang, Y.Q. Zhang, Hydrothermal synthesis of Au@SnO_2 hierarchical hollow microspheres for ethanol detection, Sens. Actuators B Chem. 319 (2020) 128299.